

# Vacuum-Healing of Grain Boundaries in Sodium-Doped CuInSe<sub>2</sub> Solar Cell Absorbers

Finn Babbe, Nicoleta Nicoara, Harvey Guthrey, Nathalie Valle, Omar Ramirez Sanchez, Damien Aureau, Hossam Elanzeery, Deepanjan Sharma, José Luís Virtuoso, Jean-Nicolas Audinot, Anastasiya Zelenina, Sevan Gharabeiki, Tom Wirtz, Susanne Siebentritt, Phillip J. Dale, Sascha Sadewasser, and Diego Colombara\*

Alkali metal doping and grain boundaries (GB) have been at the center of attention within the Cu(In,Ga)(S,Se)<sub>2</sub> photovoltaics community for years. This study provides the first experimental evidence that the GB of sodium-doped CuInSe<sub>2</sub> thin films may undertake reversible oxidation even at room temperature, whereas undoped films may not. The findings are corroborated by cathodoluminescence imaging, secondary ion mass spectrometry, and Kelvin probe force microscopy on air-exposed films subsequently subject to vacuum. A thermochemical assessment identifies the likely solid–gas equilibria involved. These reactions open new research questions with respect to the beneficial role played by alkali metal dopants in chalcopyrite solar cells and may steer the community toward new breakthroughs.

The classical explanation for the beneficial enhancement of p-type conductivity in CIGS by sodium extrinsic doping was to assume a replacement of (In<sub>Cu</sub>) antisite donor defects by neutral (Na<sub>Cu</sub>) substitutionals.<sup>[9]</sup> However, since (In<sub>Cu</sub>) defects were suggested to be highly stabilized both thermodynamically and kinetically,<sup>[10]</sup> the discussion on the extraordinary role played by sodium in CIGS was reopened.

The latest interpretation by Yuan et al.<sup>[2]</sup> focuses on the bulk of the CIGS grains. According to their model, the solubility of sodium as (Na<sub>Cu</sub>) increases at high temperatures, causing Cu to migrate out of the grains. When the samples are then

cooled down, the solubility of sodium decreases, that is, sodium is expelled from the grain interior (GI) and its excess is later removed by rinsing. The end result would be an increased concentration of copper vacancies (V<sub>Cu</sub>) in the CIGS grains, which would then explain the increased p-type doping of CIGS films exposed to sodium.

Once segregating at grain boundaries (GB), sodium was also proposed to passivate defects there.<sup>[11]</sup> However, as per the grain interior case, it is unclear how sodium could play a direct role

## 1. Introduction

Cu(In,Ga)Se<sub>2</sub> (CIGS) solar cells are the leading thin film photovoltaic technology in terms of power conversion efficiency. Yet, nearly 25 years after the seminal work by Kronik et al. on the so-called “sodium effect,”<sup>[1]</sup> and despite a triple-digit number of publications and patents on the topic, alkali metal doping of CIGS keeps stimulating intense debates as to the root mechanism of its efficiency-boosting properties.<sup>[2–8]</sup>

F. Babbe  
Chemical Sciences Division  
Lawrence Berkeley National Laboratory  
Berkeley, CA 94720, USA

F. Babbe, O. Ramirez Sanchez, H. Elanzeery, A. Zelenina, S. Gharabeiki, S. Siebentritt, P. J. Dale  
University of Luxembourg  
Physics and Materials Science Research Unit  
41 Rue du Brill, Belvaux L-4422, Luxembourg  
N. Nicoara, D. Sharma, J. L. Virtuoso, S. Sadewasser  
International Iberian Nanotechnology Laboratory  
Av. Mestre Jose Veiga, Braga 4715-330, Portugal


H. Guthrey  
National Renewable Energy Laboratory  
1617 Cole Blvd, Lakewood, CO 80401, USA

N. Valle, J.-N. Audinot, T. Wirtz  
Luxembourg Institute of Science and Technology  
Material Research & Technology Department  
41 Rue du Brill, Belvaux L-4422, Luxembourg

D. Aureau  
University of Versailles  
Institut Lavoisier  
45 Avenue des États Unis, Versailles 78000, France

H. Elanzeery, A. Zelenina  
Avancis GmbH  
Otto-Hahn-Ring 6  
81739, München, Germany

D. Colombara  
Università degli Studi di Genova  
via Dodecaneso 31, Genova 16146, Italy  
E-mail: diego.colombara@bath.edu

 The ORCID identification number(s) for the author(s) of this article can be found under <https://doi.org/10.1002/aenm.202204183>.

© 2023 The Authors. Advanced Energy Materials published by Wiley-VCH GmbH. This is an open access article under the terms of the Creative Commons Attribution License, which permits use, distribution and reproduction in any medium, provided the original work is properly cited.

DOI: 10.1002/aenm.202204183

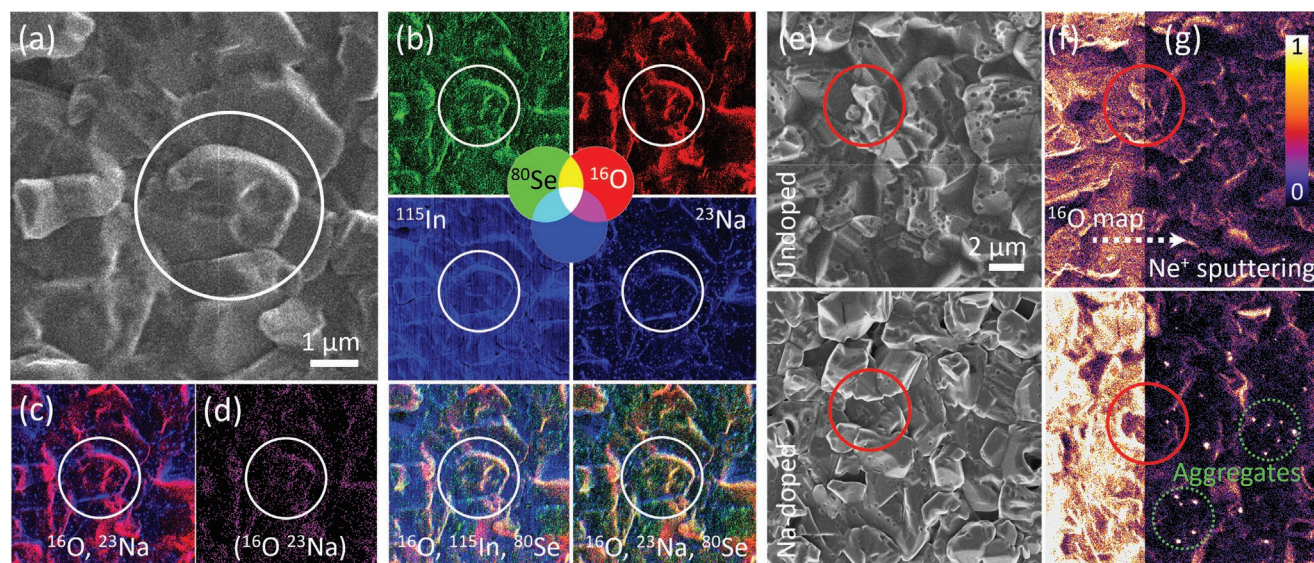


**Figure 1.** a) He-induced secondary electron micrograph of the Na-doped CIS film after 2 h of air exposure. b) Corresponding correlative SIMS elemental distributions of  $^{80}\text{Se}$  (green),  $^{16}\text{O}$  (red),  $^{23}\text{Na}$ , and  $^{115}\text{In}$  (blue), and corresponding superpositions. c) Corresponding overlay of the O (red,  $m/z = 15.995$  amu) and Na (blue,  $m/z = 22.990$  amu) SIMS images. d) Corresponding distribution of the  $(^{16}\text{O}^{23}\text{Na})$  atomic cluster measured at mass  $m/z = 38.985$  amu. e) He induced secondary electron micrographs showing the morphology of undoped (top) and Na-doped (bottom) CIS films after 2 h of air exposure and f,g) corresponding  $^{16}\text{O}$  SIMS images of the bare oxidized surface (f) and the identical surface after material removal by  $\text{Ne}^+$  sputtering (g). The same normalized intensity scale applies to SIMS images in (f) and (g). Solid circles are guides to the eye. Dashed green circles highlight the presence of aggregates with high O content in the Na-doped films. Note that the blisters in (e) are caused by He gas accumulation.<sup>[17]</sup>

from an electronic viewpoint. The pioneering chemical passivation mechanism proposed by Kronik et al. in 1998<sup>[1]</sup> suggests that sodium catalyzes the oxygenation of selenium vacancies. Selenium vacancies were proposed to otherwise form amphoteric complexes with copper vacancies in copper-poor surfaces and grain boundaries, which was recently confirmed to cause device performance losses.<sup>[12]</sup> By easing the formation of  $\text{O}_{\text{Se}}$  substitutionals, sodium helps neutralize the amphoteric defect complex, thus passivating grain boundaries.

The present research shows that sodium located at the grain boundaries of  $\text{CuInSe}_2$  (CIS) also minimizes the detrimental oxidation of indium and copper acting as sacrificial getters of molecular oxygen. This gettering reaction is a reversible solid-gas equilibrium, as revealed by secondary ion mass spectrometry (SIMS) depth profiling and nano-imaging on specimens deliberately exposed to air and subsequently subjected to ultra-high vacuum (UHV). A recently developed SIMS imaging technique on a helium ion microscope (HIM)<sup>[13,14]</sup> reveals preferential oxidation of grain boundaries and edges with a sub-20 nm resolution. The chemical composition of the surface and the reversibility of the oxygen chemisorption are analyzed by X-ray photoelectron spectroscopy (XPS), and the consequences of the equilibrium reaction on the optoelectronic properties are investigated by cathodoluminescence (CL) spectrum imaging and Kelvin probe force microscopy (KPFM).

## 2. Results and Discussion

**Figure 1** provides high spatial resolution information on the elemental distribution within the Na-doped air-exposed film acquired by HIM-SIMS. The  $^{16}\text{O}$  (red, R) and  $^{80}\text{Se}$  (green, G) SIMS

maps enable the superposition with either  $^{23}\text{Na}$  or  $^{115}\text{In}$  signal (both blue, B), leading to the corresponding RGB combinations. These show that the grain boundaries display comparatively higher intensities for both Na and In, consistent with the known segregation of Na and  $\text{CuIn}_3\text{Se}_5$  (ordered defect compound) at grain boundaries.<sup>[15,16]</sup> Some (but not all) grain boundary regions also display high O and Se SIMS signals, thus appearing white in the superposed images. The coexistence of O, Se, Na, and In in some regions is a potential sign of partial oxidation of the air-exposed CIS film. The correlation between  $^{16}\text{O}$  and  $^{23}\text{Na}$  ions yields a map (c) with magenta areas that match well with the spatial distribution of the  $(^{16}\text{O}^{23}\text{Na})$  atomic clusters removed by the primary ion bombardment and detected independently (d). The O–Na correlation suggests that O is not simply physisorbed, but chemically bound (at least to Na). The higher  $^{16}\text{O}$  signal at the grain edges is consistent with preferential reaction due to a gas phase diffusion limitation.

Surface oxidation also occurs on undoped CIS. **Figure 1e** shows the images of the undoped and Na-doped films exposed to air for 2 h, with **Figure 1f,g** showing the corresponding  $^{16}\text{O}$  ion SIMS images. The Na-doped film displays a higher  $^{16}\text{O}$  SIMS signal than the undoped film at the bare surface. Sputter-rastering of the film's surface with a 20 keV  $\text{Ne}^+$  beam reduces substantially the overall  $^{16}\text{O}$  SIMS signal. Crucially, the sputtering reveals that the Na-doped film contains submicrometer-sized zones with high O content, clearly absent in the undoped film. These submicrometer-sized zones are named aggregates thereafter.

In order to add in-depth compositional information to the bi-dimensional surface imaging of **Figure 1g**, **Figure 2** shows a series of  $^{16}\text{O}$  Nano-SIMS images acquired through the depth of the oxidized Na-doped film.  $^{16}\text{O}$  Nano-SIMS images at three different depths are selected to highlight one of the following:



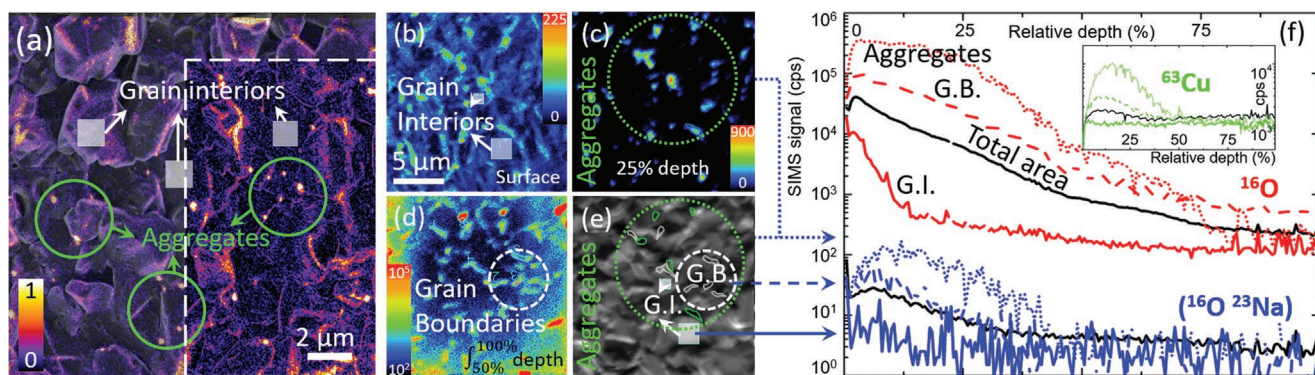


**Figure 2.** a) Laplacian pyramid fusion<sup>[23]</sup> (dashed smaller portion) and overlay (remaining portion) of the  $\text{Ne}^+$ -sputtered  $^{16}\text{O}$  SIMS image and He-induced secondary electron micrographs (shown in Figure 1e–g) corresponding to the Na-doped CIS film air-exposed for 2 h, enabling the identification of both aggregates and grain interiors. b–d)  $^{16}\text{O}$  Nano-SIMS images of the same sample (with a different instrument at a different location) obtained at the surface (b), at 25% relative depth (c), and integrated between 50% and 100% relative depth (d). e) Secondary electron image corresponding to the same area in (b–d) with highlighted grain interior (GI), grain boundaries (GB), and aggregates sites of interest. f) Cumulated area-normalized  $^{16}\text{O}$  (red) and  $(^{16}\text{O}^{23}\text{Na})$  (blue) SIMS depth profiles reconstructed from the sites of interest highlighted in (b–e). The black solid lines correspond to the total SIMS signals for the whole imaged area. The  $^{63}\text{Cu}$  depth profiles (green) are shown in the inset for clarity.

GIs (Figure 2b), aggregates (Figure 2c), and GB (Figure 2d). The ensemble of locations and corresponding  $^{16}\text{O}$  (red),  $(^{16}\text{O}^{23}\text{Na})$  (blue), and  $^{63}\text{Cu}$  (green) depth profiles are shown in Figures 2e and 2f, respectively. With the visual aid of the marking circles, it is clear that the aggregates do not necessarily occur preferentially at grain boundaries, but seem to grow (or have segregated) in their vicinity. SIMS provides semi-quantitative compositional information in the absence of calibrated standards. The aggregates yield the highest  $^{16}\text{O}$ ,  $(^{16}\text{O}^{23}\text{Na})$ , and  $^{63}\text{Cu}$  SIMS signals, followed by GB and GI. Despite a lower sensitivity for the  $(^{16}\text{O}^{23}\text{Na})$  atomic cluster, it is clear that the  $(^{16}\text{O}^{23}\text{Na})$  signal correlates spatially with  $^{16}\text{O}$  through the depth of the film. The Na–O correlation is consistent with earlier evidence in CIS and Mo,<sup>[18–21]</sup> confirmed recently in the kesterite system.<sup>[22]</sup> The  $^{63}\text{Cu}$  depth profiles also correlate with  $^{16}\text{O}$  and the  $(^{16}\text{O}^{23}\text{Na})$ , especially in the aggregates, where oxidation has occurred to the largest extent. Cu ions are known to behave similarly to alkali metal ions in a number of phases. Therefore, it is not surprising that a Cu-containing residual of CIS decomposition coexists with Na and O.

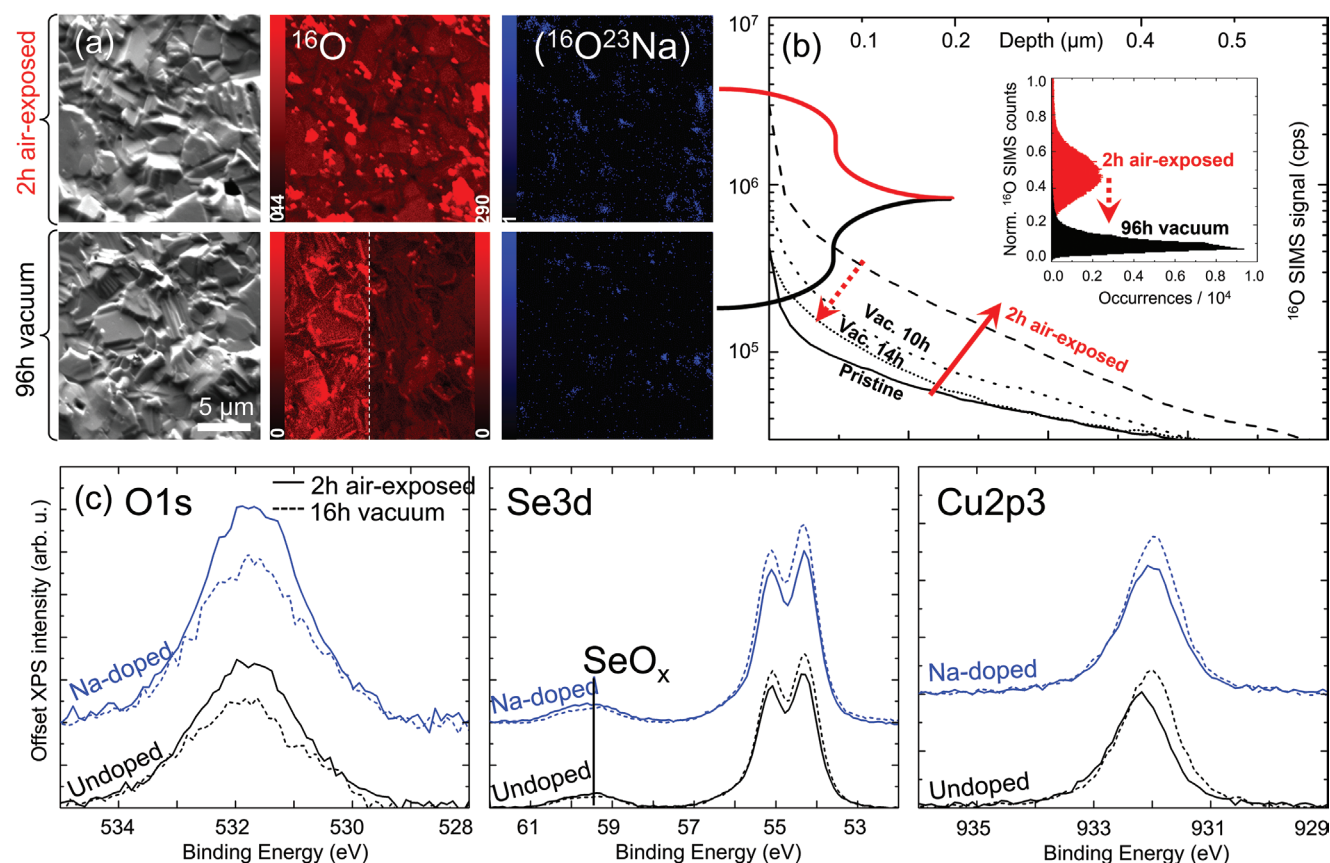
The spatial correlation between the  $^{16}\text{O}$  and the  $(^{16}\text{O}^{23}\text{Na})$  atomic cluster signals shown in Figure 3a corresponds to >90% overlap (cf. Figure S1, Supporting Information), suggesting further that O and Na are likely bound together. Exposure to vacuum reduces substantially the  $^{16}\text{O}$  signal, but the distribution of the  $(^{16}\text{O}^{23}\text{Na})$  atomic cluster signal appears unchanged. This suggests that the aggregates lose O during the vacuum treatment but still contain enough O to be detected via the  $(^{16}\text{O}^{23}\text{Na})$  atomic cluster. In order to assess the reversible nature of the oxygen loss, Figure 3b shows the  $^{16}\text{O}$  SIMS depth distribution averaged over an area of  $\approx 3000\ \mu\text{m}^2$  of a pristine Na-doped film (solid line) and after 2 h of air exposure at room temperature (dashed line). O penetrates the film to a depth of at least  $0.6\ \mu\text{m}$ , as the  $^{16}\text{O}$  SIMS signal increases by approximately one order of magnitude. The film is then left in UHV for 10 and 14 h and the O content decreases back almost to the original level (dotted lines).

Figure 3c shows the O1s, Se3d, and Cu2p3 XPS spectra of the undoped and Na-doped films after 2 h of air exposure and

subsequent 16 h of vacuum (averaged over an area of approximately ten times as large as that of the SIMS depth profiles shown in Figure 3b). Peak assignment is consistent with the extensive study by Loubat et al.<sup>[21]</sup> The O concentration of the Na-doped film is higher compared to the undoped film after air exposure, consistent with Figure 1. The Se3d signal shows two distinct contributions. The doublet at low binding energies is compatible with both CIS and elemental Se, while the peak at 59 eV binding energy is a known signature of Se–O bonds. Exposure to vacuum leads to a decrease of the O1s and Se–O peaks, while the Cu2p3 and the lower energy Se3d peaks increase. Both effects are reversible and consistent with deoxygenation of the CIS surface (In3d signal also increases with vacuum, cf. Figure S2, Supporting Information). Whereas most of the O1s signal may come from physisorbed oxygen, the higher level in the Na-doped film and the Se3d peak near 59 eV are clear signs of chemisorption.

In order to investigate the effect of deoxygenation on the optoelectronic properties of the films over a similar length scale to the imaging and SIMS measurements, CL spectrum imaging is performed on both undoped and Na-doped films after oxidation in air and subsequent exposure to a vacuum. Figure 4 shows the 300 K CL analysis of the films at identical locations before (left side of each image) and after (right side of each image) being subject to the SEM chamber vacuum for 75 h. For both films before the vacuum, the CL intensity (Figure 4a) largely depends on surface topography. GB regions exhibit weaker overall CL emission than GI, which is typically observed<sup>[24,25]</sup> also on polished samples.<sup>[26]</sup> Even within GI regions, there are large variations seemingly caused by grain roughness and extended defects. The peak energy of the emitted photons (Figure 4b) reflects only weakly the grain surface topography, but GB regions display lower peak energies, due to a higher level of compensation.<sup>[27,28]</sup> Exposure to a vacuum (right side of each image) induces meaningless changes to peak photon distribution and a very small decrease in the emission intensity (cf. Supporting Information).

The low energy side of the CL spectra is fitted with a Gaussian function aimed at extracting gamma, which is a



**Figure 3.** a) Morphology,  $^{16}\text{O}$  and  $(^{16}\text{O}^{23}\text{Na})$  atomic cluster Nano-SIMS images of a Na-doped CIS film before and after 96 h of UHV. b) Inset: pixel-by-pixel histogram distribution of normalized  $^{16}\text{O}$  counts from the SIMS maps shown in (a) before (red) and after vacuum (black). Main graph: high-resolution  $^{16}\text{O}$  SIMS depth profiles (obtained with the CAMECA SC-Ultra depth profiling instrument) of the film in its pristine state (solid), after air exposure (dashed) and after different durations of UHV (dotted lines). c) Offset O1s, Se3d, and Cu2p3 XPS spectra of undoped and Na-doped CIS films after 2 h of air exposure (solid lines) and subsequent 16 h of vacuum (dashed lines).

measure of the magnitude of potential fluctuations (cf. Supporting Information).<sup>[29]</sup> A high gamma represents broader emission peaks, implying a higher degree of potential fluctuations. Gamma is obtained for every pixel of the map, yielding the corresponding gamma maps (c). These maps clearly reveal a higher gamma mode associated with GB regions. In the Na-doped film, the effect is so pronounced that it results in a clear bimodal gamma distribution (d). Here, the majority of pixels (mainly away from grain boundaries) display a gamma parameter below 0.1 eV, whereas a second mode around 0.15 eV appears that is correlated with grain boundaries. Exposure of the undoped film to a vacuum in the SEM chamber for 75 h does not alter the gamma distribution appreciably. However, the effect in the Na-doped film is exceptional, as the higher gamma mode disappears almost completely. The effect is confirmed also for areas not previously subject to CL (cf. Figure S4, Supporting Information), suggesting that exposure to vacuum has a healing effect on GB.

CL analysis is also performed at 10 K (Figure 5a), with the aim of gaining insights into the luminescent electronic transitions. As for the 300 K measurements, the 10 K CL yield depends on the film topography (independent of roughness, cf. Figure 5b), being lower at GB compared to GI, but the overall intensity increases considerably after vacuum. Figure 5c shows

typical CL spectra of the air-exposed films before and after 75 h of vacuum. Three spectral features are clearly seen, attributed to the excitonic transition (EX: 1.03 eV) and donor–acceptor pair transitions (DA1: 0.99 eV and DA2: 0.97 eV).<sup>[30]</sup> These three emission ranges are labeled in RGB format and the corresponding maps (d) indicate their dominant spatial distribution.

The accelerating voltage for the 10 K CL analysis is one-third of that employed for the 300 K analysis. Therefore, charge carrier generation occurs closer to the film surface, making the results in Figure 5d more sensitive to surface chemical effects (cf. Figure S4, Supporting Information).<sup>[31]</sup> Exposure to vacuum clearly decreases the relative intensity of DA1 and DA2 peaks with respect to EX in the Na-doped film, while the undoped film mostly shows an overall increase in CL yield. Furthermore, there is a noticeable change in the distribution of the DA1 peak after the vacuum exposure in the Na-doped film. Prior to exposure, grain interiors are dominated by DA1 emission, whereas EX emission takes over after the exposure, with DA1 emission occurring primarily at grain boundaries. The DA2 seems unaffected by the vacuum exposure. Interestingly, the distribution of DA1, DA2, and EX emission in the undoped sample seems unaffected by the vacuum treatment.

Comparing CL and compositional inhomogeneities can help to inspect further the correlation between surface chemistry and



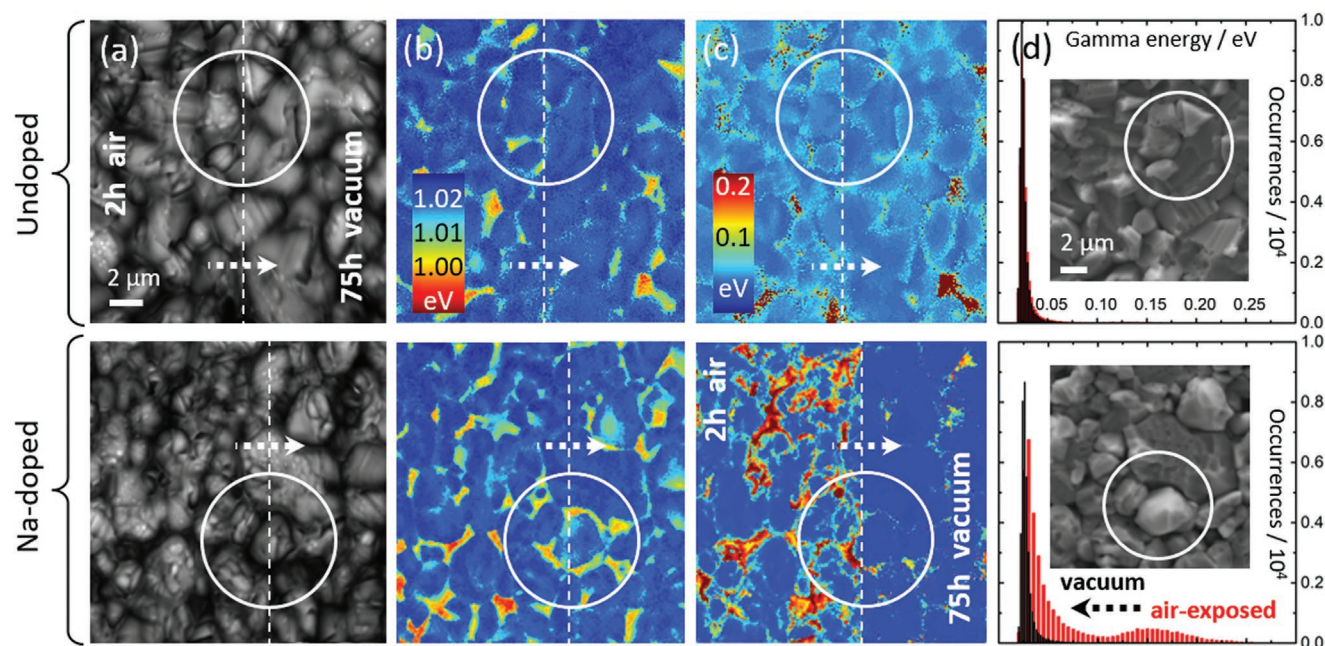


**Figure 4.** CL analysis at 300 K of the undoped and Na-doped CIS films after 2 h of air exposure (left side of each image) and after 75 h of vacuum in the SEM chamber acquired at identical locations (right side of each image). a) CL intensity maps. b) Maps of the photon energy corresponding to the CL spectral peak of intensity (same scale applies). c) Gamma parameter maps extracted by fitting the low energy side of the CL spectra at each pixel<sup>[49]</sup> (same scale applies). d) Histograms of the gamma parameter distributions. Inset: corresponding SEM micrographs of the site of interest, where the white circles indicate the same areas as in (a–c).

optoelectronic properties. **Figure 6** reports the 10 K CL map (cf. Figure 5d) and SIMS compositional distribution (cf. Figure 1b) of the Na-doped film at the same magnification (note that these analyses were not performed simultaneously, but comparing all the different methods side-by-side should bring added value). It is clear that the length scale and visual appearance of the features in Figure 6d–f are very similar. Exposure to vacuum appears to decrease the extent of DA pair transition in favor of the excitonic emission (Figure 6c,d). The removal of oxygen from the Na-doped films occurs hundreds of nm below the surface, as revealed by the SIMS depth profiling (Figure 3c), and is mostly associated with grain boundaries (cf. Figure 2f). Therefore, the reduced extent of DA1 and DA2 after the vacuum is directly or indirectly associated with oxygen removal. This fact, together with the evidence of gamma reduction after vacuum (Figure 4d), suggests that the oxygen removal from CIS surfaces and grain boundaries is beneficial, correlates with the presence of Na, and is eased by Na. The vacuum-induced CL effects are tentatively assigned to the desorption of physisorbed and chemisorbed oxygen in the undoped and Na-doped films, respectively. Considering the topographical correlation between Cu, Na, and O in the Na-doped film (cf. Figure 2f), the oxygen removal and concurrent drop of DA1 and DA2 signals suggest the chemical reversibility of the CIS decomposition. In such a hypothetical scenario, the outgrown Cu–O phase is stripped of its oxygen and results in Cu redistribution (given its high mobility),<sup>[32]</sup> which lowers the concentration of  $\text{In}_{\text{Cu}}$  defects that are likely involved as shallow donors in both DA1 and DA2 transitions.<sup>[30,33]</sup>

**Figure 7** shows the KPFM analysis of Na-doped and undoped CIS films. The analysis includes several independent grain boundaries, across which contact potential difference (CPD)

line profiles were extracted from images acquired periodically over a timeframe of >20 h under UHV. The Na-doped film shows a progressive drop of CPD signal over time while being held in a vacuum (Figure 7b,c). The CPD drop is generalized, but is manifest at grain boundary regions, as shown in Figure 7g where the CPD signal is extracted along the grain boundary only. Conversely, the undoped film reveals almost no change in the CPD profiles across the grain boundary (Figure 7e,f), or along the grain boundary (Figure 7g) and a narrower distribution of CPD over the analyzed surface area (inset). By combining this information with the other experimental techniques, it is possible to state that the variation with time of the CPD signal observed for the Na-doped film is compatible with vacuum-induced charge redistribution at the film surface, especially along the grain boundaries.

In order to account for the improvements of early CIS devices upon post-fabrication air annealing, Cahen and Noufi proposed in 1991 a model involving the passivation of ( $V_{\text{Se}}$ ) donors by oxygen via the formation of ( $O_{\text{Se}}$ ) substitutional defects.<sup>[34]</sup> It was argued that the reduction of recombination losses was directly linked to the oxygenation of selenium vacancies. Their model was later expanded by Kronik et al. when it occurred that the presence of sodium in the CIGS film diffusing from the soda lime glass (SLG) substrate made the air annealing step unnecessary.<sup>[1]</sup> A catalytic mechanism was invoked, consistent with older literature on carbon soot oxidation,<sup>[35]</sup> for which the sodium-containing segregations at the CIGS surface and grain boundaries induce polarization of the molecular oxygen bond (physisorbed on the CIGS surface, e.g., due to air exposure), easing its dissociation into atomic oxygen and subsequent capture by  $V_{\text{Se}}$ . The result was the known increased p-type



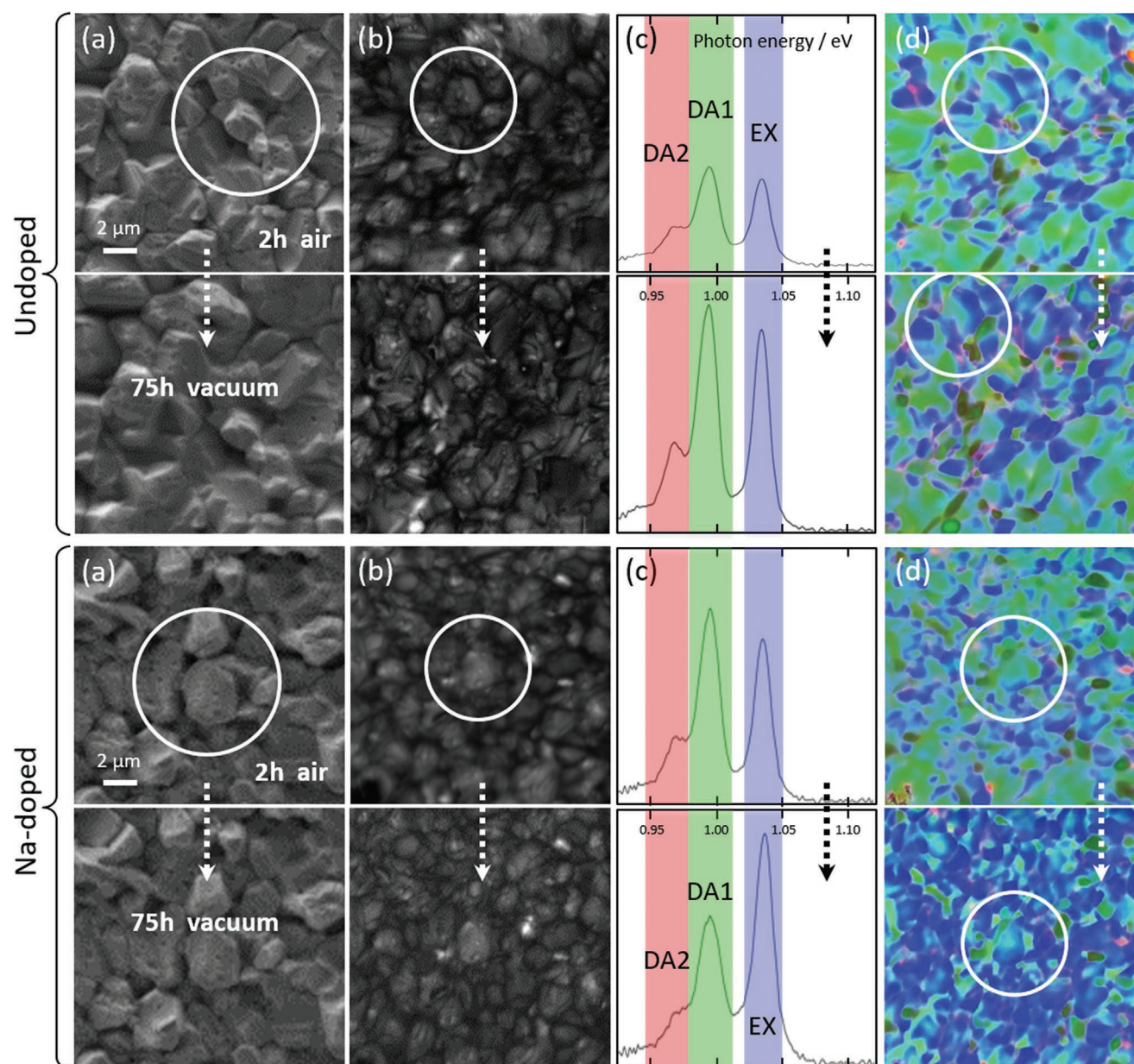


**Figure 5.** a) SEM micrograph of the undoped and Na-doped CIS films analyzed by CL at 10 K at identical locations after 2 h of air exposure (top) and after 75 h of vacuum in the SEM chamber (bottom). b) Corresponding CL intensity maps. c) CL spectra of the films averaged over the entire analyzed areas featuring three distinct emissions labeled in RGB format (same normalized intensity applies for each sample before and after vacuum). d) Corresponding RGB maps reveal the spatial distribution of the three emission ranges. The white circles are a guide to the eye for identification of the identical locations within each sample type, thus accounting for slight unintentional lateral shifts.

doping and reduced charge carrier recombination, leading to higher open circuit voltages.<sup>[36]</sup>

Unlike early CIS devices, modern absorbers contain low initial concentrations of selenium vacancies due to the improved deposition processes. Yet, it was shown that the chemical instability of the CIS surface against oxygen causes the spontaneous formation of selenium vacancies even at room temperature, especially on CIS samples grown under Cu excess.<sup>[12]</sup> As a result, whereas a short exposure to air may be beneficial, extended air annealing of bare CIGS films is detrimental for absorber/buffer interfaces, as shown by Hölscher et al.<sup>[37]</sup>

Mönig et al. have shown that 280 °C annealing under UHV leads to homogeneous current imaging tunneling spectroscopy maps on bare CIS films, while the same maps acquired on films subsequently subject to air annealing display granular inhomogeneities. They concluded that thermal annealing under UHV enables to passivate CIS surface defects and increases significantly the surface band bending leading to a prospective increase of open circuit voltage.<sup>[38]</sup> In this sense, the success of alkali metal doping seems at odds with the study by Shin et al., who clearly showed that Na and K promote oxygen chemisorption into bare CIGS films.<sup>[39]</sup>

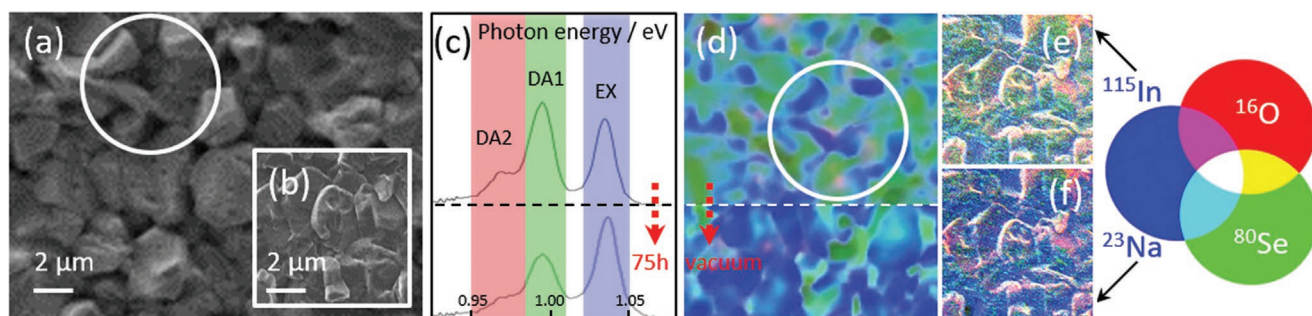


**Figure 6.** Ensemble of independent analyses displayed at the same magnification for discussion purposes. a) SEM and b) He-induced secondary electron micrographs of the Na-doped CIS film exposed to air for 2 h. c) 10 K CL spectrum of the film with labeling of the DA2 (red), DA1 (green), and excitonic (blue) transitions. d) Correspondingly colored CL emission map at 10 K. e, f) SIMS imaging of (b) with overlaid  $^{16}\text{O}$  (red),  $^{80}\text{Se}$  (green), and either  $^{115}\text{In}$  (e) or  $^{23}\text{Na}$  (f) (blue) signals.

These seeming contradictions are reconciled by the present study. The phenomenon observed by Mönig et al.<sup>[38]</sup> may relate to the vacuum-induced deoxidation of the CIS surface, demonstrated here at room temperature. Air exposure of bare CIS leads to the formation of mostly indium oxides—according to experimental observation<sup>[40]</sup>—but also copper oxides, according to thermochemical equations. In this study, air exposure of CIS in the absence of sodium leads to lower luminescence yields and higher overall electrostatic potential fluctuations. If Na is present in the films, oxygen incorporation may be enhanced, in accordance with Shin et al.<sup>[39]</sup> However, CIS decomposition into In and Cu oxides may be curbed thanks to the preferential formation of Na–O phases segregating into aggregates (cf. Figure 2), leading to high electrostatic potential fluctuations at the grain boundaries. These phases appear to be amenable to de-oxidation upon exposure of the films to vacuum, healing the gamma parameter at grain boundaries, as revealed by CL (cf. Figure 4c). The reversible nature of these equilibria is consistent with thermochemical equations shown in Figure 8a,b and with the phenomenological interpretation described in Figure 8c,d.

Previous findings indicate that oxygen initially passivates  $V_{\text{Se}}$  at the CIS surface, exerting a beneficial action, and then induces the formation of In–O and Cu–Se, generating the  $V_{\text{Cu}}\text{--}V_{\text{Se}}$  complex.<sup>[12]</sup> Hence, the phenomenological interpretation is that once  $\text{O}_{\text{Se}}$  defects are formed, they can shuffle O to other more thermodynamically favorable locations, as supported by Sahoo et al.<sup>[42]</sup> In the case of undoped CIS, the path leads to the irreversible growth of In–O, especially at grain boundaries.<sup>[12]</sup> This is even supported by a recent study where undoped air-exposed epitaxial CIS films subject to annealing at 200 °C under UHV reveal irreversible alteration of the work function.<sup>[44]</sup> Na doping, instead, was already suggested to catalyze In–O bond formation,<sup>[1,34]</sup> but it is argued here that it may also act as a sacrificial oxygen buffer by forming Na–O phases. Now, even though the growth of Na–O phases is unlikely to prevent the detrimental formation of the divacancy complex (chemical equations in Figure 8c), the lower free energy involved ensures that the process is reversible. Upon application of vacuum, it is then possible to revert Na and O back into the CIS phase to re-passivate the divacancy complex, which would account for the drop of gamma parameter observed in the CL map (if the complex is present in its donor configuration) and for the drop of the DA1 PL peak. The equations in Figure 8a,b do not consider the role

of moisture because its effect on the energetics of ion hydration is not trivial. Nevertheless, water is likely to play a crucial role in speeding up the sacrificial oxygen gettering, as the reaction is consistent with the observed drop of resistivity in Na-doped CIGS upon exposure to (moist) air rather than pure oxygen,<sup>[45]</sup> a sign of electrical ionic conduction across grains.

### 3. Conclusions

This study shows that Na doping minimizes the detrimental decomposition of CIS upon exposure to air and heals oxidized grain boundaries with positive effects on the radiative recombination of the bare absorbers. It confirms the catalytic effect invoked 25 years ago by Kronik to explain the Na-enhanced oxygen incorporation into CIS<sup>[1]</sup> and posits that oxygen desorption from CIS may simply be the consequence of the catalytic effect exerted by alkali metal dopants in the opposite direction. This hypothesis unites previous studies with seemingly contradicting results. Future research will be devoted to testing the hypothesis, especially on heavier alkali metal dopants,<sup>[46]</sup> and to identify the link between the reversibility of oxidation and the chemical processes happening in the liquid phase still encountered during most baseline solar cell finishing.<sup>[36,47]</sup> Likewise, the impact on device performance will have to be assessed.

### 4. Experimental Section

**Sample Preparation and Surface Treatments:** The CIS absorbers were fabricated by physical vapor deposition in a molecular beam epitaxy system at 530 °C using a 1-stage co-evaporation process. The substrates employed were Mo-coated SLG (Na-doped films) that in the case of undoped films also comprised an alkali metal diffusion barrier between the glass and the Mo layer. The as-prepared CIS films grown under Cu excess were etched in a KCN 10 wt% aqueous solution for 5 min in order to remove any residual Cu–Se phase that may have formed during the growth, leading to a Cu/In atomic ratio of  $1.07 \pm 0.05$  measured by energy-dispersive X-ray spectroscopy (EDS), that is, an essentially stoichiometric CIS.<sup>[12]</sup> The films were then exposed to air and analyzed either with the shortest possible delay (transfer times  $\approx 5$  min) or intentionally left in air for up to 24 h under dark conditions to ensure a reproducible “oxidized” surface state. Subsequently, the films were analyzed under each technique’s typical vacuum environment (Table 1) as soon as allowed, and after various periodic intervals, as described in the manuscript.



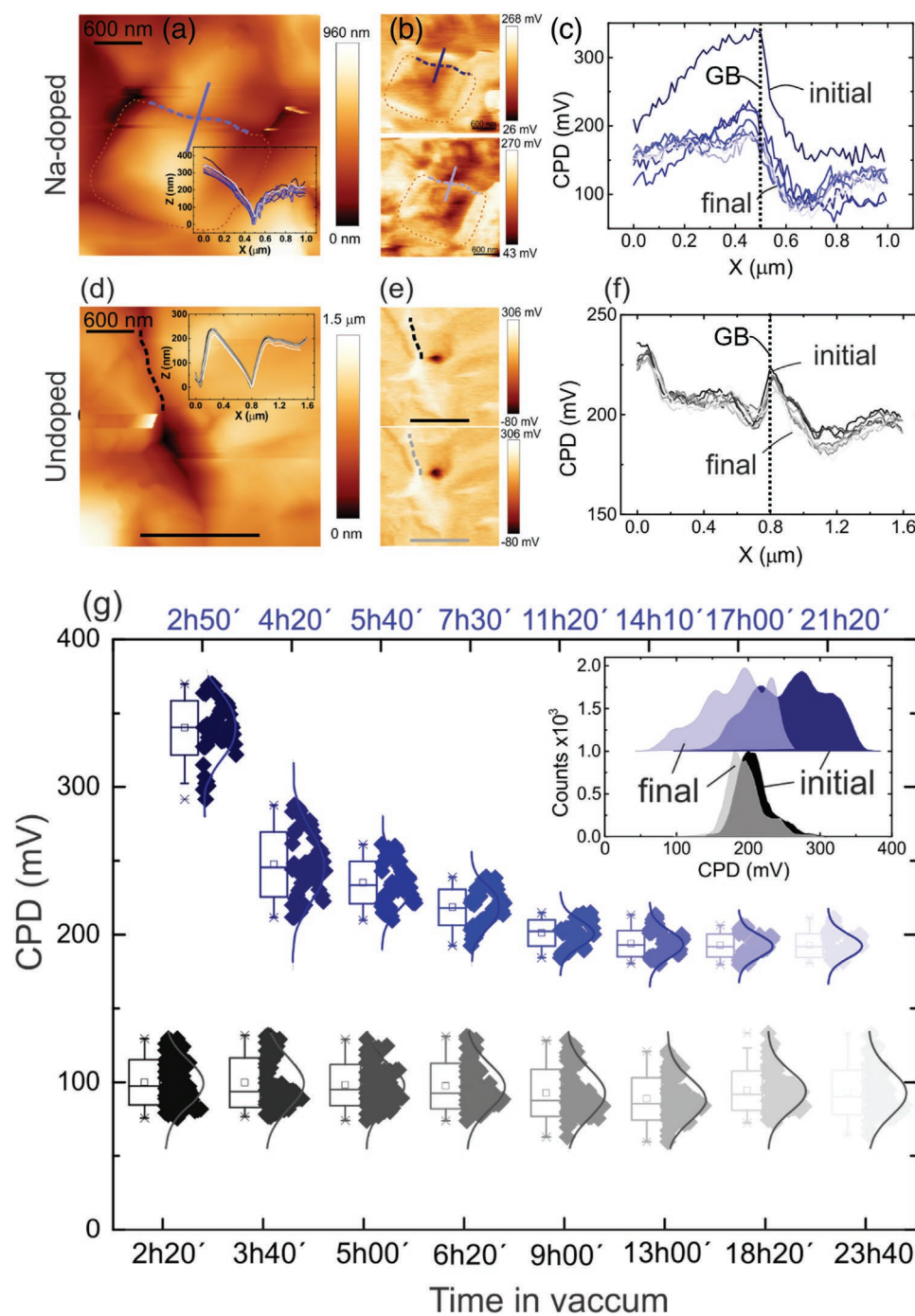


**Figure 7.** Topography image of the Na-doped (a) and undoped (d) air-exposed CIS films. Corresponding contact potential difference (CPD) maps (b,e) at the beginning (top) and end of acquisition (bottom). The CPD line scans across the grain boundaries indicated by the solid lines in (b) and (e) are shown in (c) and (f), respectively, for various exposure times under UHV (dark to light). g) Distribution of CPD values along the grain boundaries indicated by the dashed lines in (b) and (e) as a function of exposure time under UHV. Inset: overall CPD distributions extracted from the initial (dark) and final (light) image acquisitions of the Na-doped (top) and undoped (bottom) CIS films.

**Helium and Secondary Ion Mass Spectrometry Imaging:** Helium and neon-induced secondary electron microscopy and SIMS images were acquired with an HIM (Zeiss, Peabody (US)) coupled with an add-on SIMS system (LIST, Luxembourg)<sup>[13,14]</sup> (cf. Figure 1 also reported in Figures 2a and 6b,e,f). In this case study, the HIM-SIMS images were acquired with a 20 keV helium beam of 0.5 pA and a 20 keV neon beam of 2 pA, respectively. The secondary ions were collected

and detected in both polarities. The SIMS images were recorded for a matrix of  $512 \times 512$  pixels and with a counting time of 3 ms/pixel. In these conditions, a sub-20 nm lateral resolution was expected for SIMS analysis. The air-exposed CIS film was analyzed twice at an identical location, before and after  $\approx 18$  h under vacuum ( $10^{-7}$  mbar) in the HIM chamber and for comparison on an area not scanned initially.



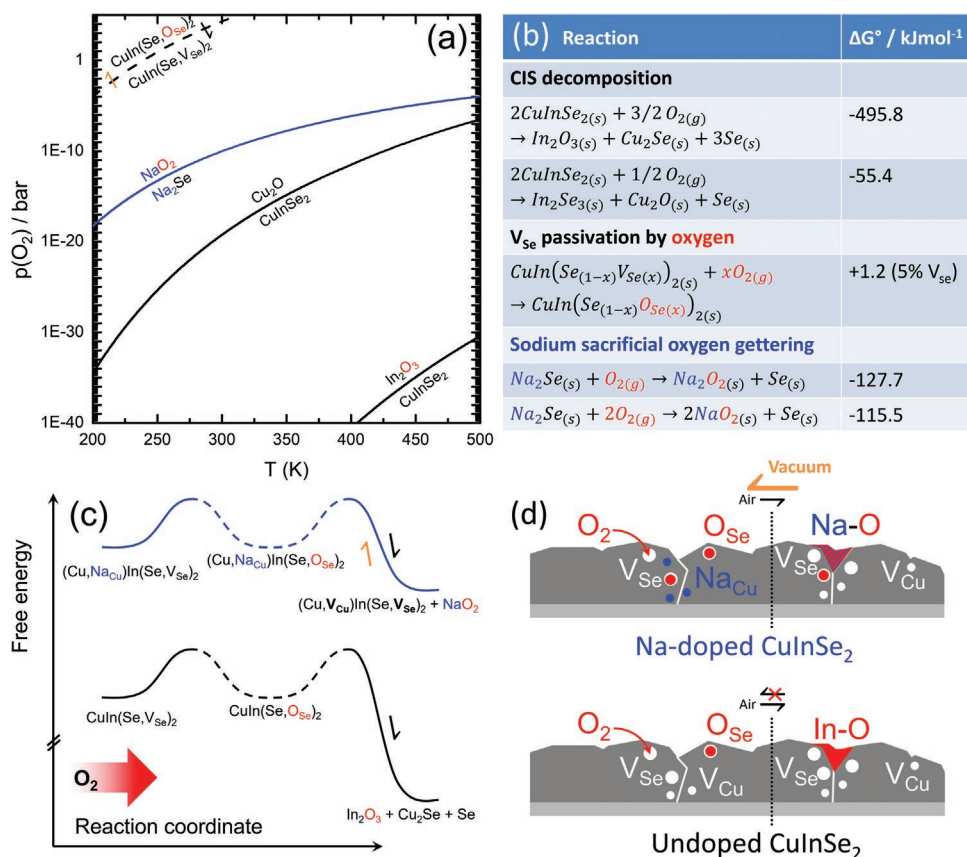


**Figure 8.** a) Temperature–pressure ( $\text{O}_2$ ) diagrams of chemical equilibria involving CIS decompositions (solid black curves) and O-uptake/release by defected CIS (black dashed), and relevant sodium (blue) phases. b) Corresponding standard Gibbs free energies calculated from refs. [41,33,42,43]. c) Tentative energy diagram inspired by refs. [12,34] and d) sketch acknowledging the (ir)reversibility of grain boundary oxidation in the Na-doped (undoped) CIS film including its consequences on point defect passivation/formation.

**Secondary Ion Mass Spectrometry:** The SIMS technique was used in two modes: depth profiling and nano-imaging. The depth profiling was carried out on a CAMECA SC-Ultra instrument (CAMECA, France) with a 1 keV  $\text{Cs}^+$  beam. Secondary negative ions (e.g.,  $^{16}\text{O}^-$ ) were collected from an area of  $60 \mu\text{m}$  in diameter center on a  $(200 \times 200) \mu\text{m}^2$  sputtered area. After 2-h of air exposure, the Na-doped CIS film was rapidly introduced in the SC-Ultra analysis chamber and then stored in a vacuum of about  $8 \times 10^{-9}$  mbar for successive in-depth analyses (main graph in Figure 3b). A CAMECA NanoSIMS 50 (CAMECA, France) was used to acquire 3D (Figure 2b–f) and 2D (Figure 3a) SIMS images. These images were acquired with a 16 keV  $\text{Cs}^+$  beam of 1.5 pA for studying the distribution of  $^{16}\text{O}^-$ , ( $^{16}\text{O}^{23}\text{Na}$ ) $^-$  atomic cluster,  $^{63}\text{Cu}^-$  and  $^{78}\text{Se}^-$  simultaneously in multicollection mode. The Nano-SIMS images

**Table 1.** Summary of vacuum exposure conditions, duration, and relevant figures.

Technique	Vacuum	Duration [h]	Figure
HIM-SIMS	$10^{-7}$ mbar	18	1
SIMS NanoSIMS 50	$10^{-9}$ mbar	96	3a, 3b (inset)
SIMS SC-Ultra	$8 \times 10^{-9}$ mbar	10, 14	3b
XPS	$10^{-7}$ mbar	16	3c
XPS	$10^{-7}$ mbar	Up to 88	S2, Supporting Information
CL	$10^{-7}$ mbar	75	4, 5
KPFM	$4 \times 10^{-11}$ mbar	>20	7

were recorded for a matrix of  $256 \times 256$  pixels and with a counting time of 10 ms/pixel. The size of the images was  $(20 \times 20) \mu\text{m}^2$ . The size of the beam was adjusted to 150 nm as a good compromise between the sputtering rate (reasonable acquisition time to image the whole oxidized layer) and the lateral image resolution. The analysis chamber pressure was  $\approx 1 \times 10^{-9}$  mbar.

**Cathodoluminescence Analysis:** The CL analysis was performed with an acceleration voltage of 15 (at 300 K) and 5 kV (at 10 K) and a beam current of  $\approx 1$  nA over a scanned area of  $15 \times 15 \mu\text{m}^2$ ,  $200 \times 200$  pixels. The analysis of the air-exposed CIS film was repeated at the identical location after  $\approx 75$  h in an SEM chamber vacuum and for comparison on a region not scanned initially, in order to exclude measurement artifacts. The CL emission intensity images were panchromatic and formed from all emissions from the samples. The pixel color in the CL emission energy maps resulted from segmenting the emission spectrum into various energy channels (indicated in the accompanying spectra), normalizing the intensity of each pixel, and then summing the contributions of the red, green, and blue channels to determine the RGB value of each pixel. The red/green/blue color scheme was chosen because it was easy to understand the images qualitatively in terms of lower (red) to higher (blue) energy emissions.

**Kelvin Probe Force Microscopy:** KPFM experiments were performed in a UHV scanning probe microscope (SPM), Omicron Nanotechnology GmbH, controlled by Nanonis electronics and using a PtIr-coated cantilever ( $f_0 = 167$  kHz). Amplitude modulation (AM) was used for the detection of the CPD with an ac bias of 400 mV at the 2nd oscillation mode of the cantilever. In this setup, the CPD was defined as  $\text{CPD} = \Phi_{\text{sample}} - \Phi_{\text{tip}}$ .

The samples were air-exposed for  $\approx 22$  h and then loaded into the pre-vacuum chamber (where a decrease from atmospheric pressure

to  $\approx 2 \times 10^{-8}$  mbar occurs within  $\approx 18$  h), before being transferred into the analysis chamber (with a pressure of  $\approx 4 \times 10^{-11}$  mbar). KPFM was used to locally probe the changes in the CIS surface potential, by monitoring the spatially resolved CPD in a time-dependent study. The acquisition time of a KPFM measurement, consisting of a topographic and a CPD image was  $\approx 1$  h and 30 min. A continuous scan of an identical area of the sample with  $3 \mu\text{m} \times 3 \mu\text{m}$  size was performed over  $\approx 23$  h and 40 min for the undoped-CIS sample and over  $\approx 21$  h and 20 min for the Na-doped CIS sample. The identification of grain boundaries was performed according to the methodology described in ref. [48].

**X-Ray Photoelectron Spectroscopy:** The XPS spectrometer used was a Thermo Scientific Nexsa X-Ray System. Data were acquired using an Al  $K\alpha_1$  monochromatic X-ray excitation. The photoelectrons were collected perpendicularly to the sample surface over an elliptical spot with a major axis of  $400 \mu\text{m}$ . The detection was performed in a constant analyzer energy mode (CAE), using a step of  $0.1 \text{ eV}$  and a pass energy of  $20 \text{ eV}$ . For aging measurements, the samples remained in the analysis chamber under a pressure of about  $10^{-7}$  mbar. The data was processed using the Thermo Electron "Avantage XPS software."

## Supporting Information

Supporting Information is available from the Wiley Online Library or from the author.

## Acknowledgements

This study was enabled by the Fonds National de la Recherche (FNR, Luxembourg) in the framework of the GALDOCHS project (Gas-phase alkali doping of chalcogenide semiconductors, C14/MS/8302176), and by the University of Genova in the framework of the Curiosity-Driven project EDICT (Effective doping of chalcopyrite), which are gratefully acknowledged. HIM-SIMS analyses were performed in the SOLARD4D project, INTER/SNF/16/11534230, whereas other SIMS measurements (Nano-SIMS and SC-Ultra) were carried out in the framework of the GALDOCHS project. INL and the European Commission are acknowledged for funding the Nano Train for Growth II project n. 713640 through the Marie Curie Cofund program. Brahime El Adib and Esther Lentzen (LIST) are gratefully acknowledged for their support with SIMS analyses. D.C. wishes to thank the organizers, chairs and attendees of the 46th IEEE PVSC held in Chicago in June 2019 for comments and feedback on the initial findings of this study.<sup>[50]</sup>

Open access funding provided by Universita degli Studi di Genova within the CRUI-CARE agreement.

## Conflict of Interest

The authors declare no conflict of interest.

## Author Contributions

D.C. designed the research and wrote the manuscript in conjunction with all co-authors. H.G. performed the cathodoluminescence analyses and provided data interpretation in conjunction with D.C. and Su.S. N.V. first observed the experimental evidence of vacuum-induced oxygen desorption by SIMS and was in charge of the SIMS processing data with input from D.S. and D.C. O.R.S., H.E., and F.B. coordinated specimens handling/air-exposure and fabricated the  $\text{CuInSe}_2$  samples in conjunction with A.Z. The HIM-SIMS analysis was performed by J.-N.A., who interpreted the data in conjunction with T.W., N.V., D.C., and P.J.D. The KPFM analysis was performed by N.N. and D.S. who interpreted

the data in conjunction with D.C. and Sa.S. O.R.S., J.L.V., and S.G. took over sample preparation for the revision of the study. The XPS data acquisition and interpretation were performed by D.A. and D.C.

## Data Availability Statement

The data that support the findings of this study are available from the corresponding author upon reasonable request.

## Keywords

alkali metal post-deposition treatment,  $\text{Cu(In,Ga)Se}_2$ , electrostatic potential fluctuations, grain boundaries, photovoltaics

Received: December 7, 2022

Revised: February 20, 2023

Published online:

- [1] L. Kronik, D. Cahen, H. W. Schock, *Adv. Mater.* **1998**, *10*, 31.
- [2] Z. Yuan, S. Chen, Y. Xie, J.-S. Park, H. Xiang, X.-G. Gong, S.-H. Wei, *Adv. Energy Mater.* **2016**, *6*, 1601191.
- [3] A. Chirilă, P. Reinhard, F. Pianezzi, P. Bloesch, A. R. Uhl, C. Fella, L. Kranz, D. Keller, C. Gretener, H. Hagendorfer, D. Jaeger, R. Erni, S. Nishiwaki, S. Buecheler, A. N. Tiwari, *Nat. Mater.* **2013**, *12*, 1107.
- [4] P. Jackson, R. Wuerz, D. Hariskos, E. Lotter, W. Witte, M. Powalla, *Phys. Status Solidi RRL* **2016**, *10*, 583.
- [5] D. Colombara, F. Werner, T. Schwarz, I. C. Infante, Y. Fleming, N. Valle, C. Spindler, E. Vacchieri, G. Rey, M. Guennou, M. Bouttemy, A. G. Manjón, I. P. Alonso, M. Melchiorre, B. El Adib, B. Gault, D. Raabe, P. J. Dale, S. Siebentritt, *Nat. Commun.* **2018**, *9*, 826.
- [6] D. Colombara, *Phys. Rev.* **2019**, *3*, 054602.
- [7] B. J. Stanbery, D. Abou-Ras, A. Yamada, L. Mansfield, *J. Phys. D: Appl. Phys.* **2021**, *55*, 173001.
- [8] D. Colombara, K. Conley, M. Malitckaya, H.-P. Komsa, M. J. Puska, *J. Mater. Chem. A* **2020**, *8*, 6471.
- [9] S.-H. Wei, S. B. Zhang, A. Zunger, *J. Appl. Phys.* **1999**, *85*, 7214.
- [10] L. E. Oikkonen, M. G. Ganchenkova, A. P. Seitonen, R. M. Nieminen, *J. Appl. Phys.* **2013**, *114*, 083503.
- [11] A. Laemmle, R. Wuerz, T. Schwarz, O. Cocjaru-Mirédin, P.-P. Choi, M. Powalla, *J. Appl. Phys.* **2014**, *115*, 154501.
- [12] D. Colombara, H. Elanzeery, N. Nicoara, D. Sharma, M. Claro, T. Schwarz, A. Koprek, M. H. Wolter, M. Melchiorre, M. Sood, N. Valle, O. Bondarchuk, F. Babbe, C. Spindler, O. Cocjaru-Mirédin, D. Raabe, P. J. Dale, S. Sadewasser, S. Siebentritt, *Nat. Commun.* **2020**, *11*, 3634.
- [13] T. Wirtz, D. Dowsett, P. Philipp, in *Helium Ion Microscopy* (Eds.: G. Hlawacek, A. Götzhäuser), Springer International Publishing, Springer, New York **2016**, pp. 297–323.
- [14] D. Dowsett, T. Wirtz, *Anal. Chem.* **2017**, *89*, 8957.
- [15] O. Cocjaru-Mirédin, P. Choi, R. Wuerz, D. Raabe, *Ultramicroscopy* **2011**, *111*, 552.
- [16] D. Keller, S. Buecheler, P. Reinhard, F. Pianezzi, B. Bissig, R. Carron, F. Hage, Q. Ramasse, R. Erni, A. N. Tiwari, *Appl. Phys. Lett.* **2016**, *109*, 153103.
- [17] F. I. Allen, P. Hosemann, M. Balooch, *Scr. Mater.* **2020**, *178*, 256.
- [18] D. W. Niles, M. Al-Jassim, K. Ramanathan, *J. Vac. Sci. Technol., A* **1999**, *17*, 291.
- [19] R. V. Forest, E. Eser, B. E. McCandless, R. W. Birkmire, J. G. Chen, *AIChE J.* **2014**, *60*, 2365.



- [20] T. Hölscher, S. Förster, T. Schneider, M. Maiberg, W. Widdra, R. Scheer, *Appl. Phys. Lett.* **2017**, *111*, 011604.
- [21] A. Loubat, S. Béchu, M. Bouttemy, J. Vigneron, D. Lincot, J.-F. Guillemoles, A. Etcheberry, *J. Vac. Sci. Technol., A* **2019**, *37*, 041201.
- [22] S. Grini, K. V. Sopiha, N. Ross, X. Liu, T. S. Bjørheim, C. Platzer-Björkman, C. Persson, L. Vines, *Adv. Energy Mater.* **2019**, *9*, 1900740.
- [23] F. Vollnhals, J.-N. Audinot, T. Wirtz, M. Mercier-Bonin, I. Fourquaux, B. Schroepel, U. Kraushaar, V. Lev-Ram, M. H. Ellisman, S. Eswara, *Anal. Chem.* **2017**, *89*, 10702.
- [24] G. Hanna, T. Glatzel, S. Sadewasser, N. Ott, H. P. Strunk, U. Rau, J. H. Werner, *Appl. Phys. A* **2006**, *82*, 1.
- [25] H. Guthrey, J. Moseley, J. Nishinaga, H. Shibata, H. Takahashi, M. Al-Jassim, *IEEE J. Photovoltaics* **2018**, *8*, 1833.
- [26] D. Abou-Ras, M. Bär, R. Caballero, R. Gunder, C. Hages, M. D. Heinemann, C. A. Kaufmann, M. Krause, S. Levchenko, R. Mainz, J. Márquez, A. Nikolaeva, A. Redinger, N. Schäfer, S. Schorr, H. Stange, T. Unold, R. G. Wilks, *Sol. Energy* **2018**, *170*, 102.
- [27] U. Rau, *Phys. Rev. B* **2007**, *76*, 085303.
- [28] M. J. Romero, H. Du, G. Teeter, Y. Yan, M. M. Al Jassim, *Phys. Rev. B* **2011**, *84*, 165324.
- [29] E. O. Kane, *Phys. Rev.* **1963**, *131*, 79.
- [30] N. Rega, S. Siebentritt, J. Albert, S. Nishiwaki, A. Zajogin, M. Ch Lux-Steiner, R. Kniese, M. J. Romero, *Thin Solid Films* **2005**, *480–481*, 286.
- [31] D. Drouin, A. R. Couture, D. Joly, X. Tastet, V. Aimez, R. Gauvin, *Scanning* **2007**, *29*, 92.
- [32] L. E. Oikkonen, M. G. Ganchenkova, A. P. Seitonen, R. M. Nieminen, *J. Appl. Phys.* **2013**, *113*, 133510.
- [33] M. Malitckaya, H.-P. Komsa, V. Havu, M. J. Puska, *Adv. Electron. Mater.* **2017**, *3*, 1600353.
- [34] D. Cahen, R. Noufi, *Sol. Cells* **1991**, *30*, 53.
- [35] D. W. McKee, D. Chatterji, *Carbon* **1975**, *13*, 381.
- [36] L. Kronik, U. Rau, J.-F. Guillemoles, D. Braunger, H.-W. Schock, D. Cahen, *Thin Solid Films* **2000**, *361–362*, 353.
- [37] T. Hölscher, T. Schneider, M. Maiberg, R. Scheer, *Prog. Photovoltaics* **2018**, *26*, 934.
- [38] H. Mönig, D. Lockhorn, N. Aghdassi, A. Timmer, C. A. Kaufmann, R. Caballero, H. Zacharias, H. Fuchs, *Adv. Mater. Interfaces* **2014**, *1*, 1300040.
- [39] D. Shin, J. Kim, T. Gershon, R. Mankad, M. Hopstaken, S. Guha, B. T. Ahn, B. Shin, *Sol. Energy Mater. Sol. Cells* **2016**, *157*, 695.
- [40] J. Lehmann, S. Lehmann, I. Laueremann, T. Rissom, C. A. Kaufmann, M. Ch Lux-Steiner, M. Bär, S. Sadewasser, *J. Appl. Phys.* **2014**, *116*, 233502.
- [41] O. Knacke, O. Kubaschewski, *Thermochemical Properties of Inorganic Substances*, Springer-Verlag, Verlag Stahleisen, Berlin, New York, Düsseldorf **1991**.
- [42] S. K. Sahoo, R. K. M. Raghupathy, T. D. Kühne, H. Mirhosseini, *J. Phys. Chem. C* **2018**, *122*, 21202.
- [43] D. Cahen, R. Noufi, *J. Phys. Chem. Solids* **1992**, *53*, 991.
- [44] E. M. Lanzoni, T. Gallet, C. Spindler, O. Ramírez, C. K. Boumenou, S. Siebentritt, A. Redinger, *Nano Energy* **2021**, *88*, 106270.
- [45] J. Lee, L. Chen, U. Obahiagbon, C. Thompson, W. N. Shafarman, R. W. Birkmire, in *2013 IEEE 39th Photovoltaic Specialists Conf. (PVSC)*, IEEE, Piscataway, NJ **2013**, pp. 0398–041.
- [46] S. Siebentritt, E. Avancini, M. Bär, J. Bombsch, E. Bourgeois, S. Buecheler, R. Carron, C. Castro, S. Duguay, R. Félix, E. Handick, D. Hariskos, V. Havu, P. Jackson, H.-P. Komsa, T. Kunze, M. Malitckaya, R. Menozzi, M. Nesladek, N. Nicoara, M. Puska, M. Raghuvanshi, P. Pareige, S. Sadewasser, G. Sozzi, A. N. Tiwari, S. Ueda, A. Vilalta-Clemente, T. P. Weiss, F. Werner, et al., *Adv. Energy Mater.* **2020**, *10*, 1903752.
- [47] S. Béchu, A. Loubat, M. Bouttemy, M. Balestrieri, S. Gaiaschi, T. Hildebrandt, V. Archard, M. Frégnaux, D. Aureau, J. Vigneron, F. Donsanti, M. Jubault, P. Chapon, D. Lincot, J.-F. Guillemoles, A. Etcheberry, *2018 IEEE Proceedings of the 7th World Conference on Photovoltaic Energy Conversion (WCPEC) (A Joint Conference of 45th IEEE PVSC, 28th PVSEC & 34th EU PVSEC)*, **2018**.
- [48] N. Nicoara, T. Lepetit, L. Arzel, S. Harel, N. Barreau, S. Sadewasser, *Sci. Rep.* **2017**, *7*, 41361.
- [49] S. A. Jensen, S. Glynn, A. Kanevce, P. Dippo, J. V. Li, D. H. Levi, D. Kuciauskas, *J. Appl. Phys.* **2016**, *120*, 063106.
- [50] D. Colombara, J.-N. Audinot, D. Aureau, F. Babbe, P. J. Dale, H. Elanzeery, H. Guthrey, N. Nicoara, S. Sadewasser, D. Sharma, N. Valle, T. Wirtz, A. Zelenina, *2019 IEEE Proceedings of the 46th Photovolt. Spec. Conf., PVSC, Chicago, USA*, **2019**, pp. 0182–0184.